Materials Advances

PAPER

View Article Online
View Journal

Cite this: DOI: 10.1039/d6ma00183a

Influence of polycation modification on droplet size and internal structure in RNA/poly-L-lysine coacervates

Alba Ledesma-Fernandez,[a] Victor Krivenkov,[ab] Yury Rakovich[abcd] and Paula Malo de Molina *[a]

Received 8th February 2026,
Accepted 4th June 2026

DOI: 10.1039/d6ma00183a

rsc.li/materials-advances

Complex coacervation between RNA and poly(L-lysine) (PLL) provides a minimal and tunable model system to study biomolecular condensates and nucleic acid complexation for gene delivery. Here, we compare coacervates formed with linear PLL, hydrophobically modified PLL, and compact PLL nanoparticles to study the effect of polycation architecture and charge density. Droplet formation and size distributions are characterized by dynamic light scattering and confocal microscopy. Fluorescence confocal microscopy, using independently labelled fluorescein-RNA and rhodamine-PLL, demonstrates co-localization of both components with enhanced fluorescence quenching upon PLL modification, consistent with a reduced average separation between the two species. Fluorescence lifetime analysis shows a systematic decrease in the fluorescein lifetime from linear PLL to modified PLL and PLL nanoparticles, supporting increasingly close RNA–PLL proximity. Consistently, small-angle X-ray scattering (SAXS) indicates that all coacervates behave as strongly screened semidilute polyelectrolyte complexes, with nanometre-scale correlation lengths that decrease systematically upon PLL modification, reflecting a tighter internal organization. Together, these results demonstrate that increasing polycation compactness and lower charge density lead to tighter internal organization of RNA–PLL coacervates and highlight the complementarity of SAXS and fluorescence lifetime measurements for resolving nanoscale structure in complex coacervates.

Introduction

Liquid–liquid phase separation (LLPS) plays a central role in the formation of membraneless compartments in biological systems, such as nucleoli, stress granules, and P-bodies with important roles in gene regulation.[1] These condensates, often enriched in nucleic acids[2] and intrinsically disordered proteins or peptides,[3] exhibit dynamic and reversible assembly driven primarily by electrostatic and multivalent interactions.[4] The intrinsic complexity of biological systems makes their understanding challenging.[5] Therefore, in recent years, coacervate-based mimetic systems have proven valuable for identifying the minimal physical requirements for condensate formation and for exploring how polymer charge, flexibility, and sequence influence phase stability and material properties.[6–8]

Beyond their relevance as simplified models of biomolecular condensates, RNA–polycation complexes are also of considerable interest in the context of nucleic acid delivery. In particular, PLL-based nucleic acid complexes have been extensively explored as model systems for gene delivery and RNA packaging because their physicochemical properties can be systematically tuned through polymer chemistry and architecture.[9,10]

At the most fundamental level, polyelectrolyte complex (PEC) coacervates constitute the simplest and best-understood models of LLPS, providing a robust framework to rationalize phase behaviour in terms of electrostatics, polymer–solvent interactions, and entropic contributions.[11–13] Building on this foundation, increasing levels of biological realism have been introduced by modifying each of the charged components—for instance, varying the charge density,[14,15] replacing synthetic polyanions with RNA[16,17] or systematic variations in polypeptide or protein sequence have been used to explore how charge patterning, hydrophobicity, and chemical heterogeneity affect coacervation.[8,18] However, changes in sequence inherently couple multiple parameters, including charge density, flexibility, and local interactions, complicating the isolation of specific physical contributions.

---

[a] Centro de Física de Materiales (CFM-MPC), CSIC-EHU, 20018 Donostia-San, Spain
[b] Polymers and Materials: Physics, Chemistry and Technology, Chemistry Faculty, University of the Basque Country (UPV/EHU), 2018 Donostia-San Sebastián, Spain
[c] Donostia International Physics Center(DIPC), 2018 Donostia-San Sebastián, Spain
[d] IKERBASQUE – Basque Foundation for Science, 48009 Bilbao, Spain

The influence of polycation architecture on complex coacervation remains poorly understood. Here, architecture encompasses differences in molecular connectivity, chain compaction, and spatial organization of charges within the polycation. While some polymer architectures such as comb or bottlebrush polyelectrolytes can destabilize coacervates by effectively diluting charge density along the backbone,[19] recent work on lightly branched star polyelectrolytes has shown that increasing spatial charge density can instead enhance salt stability, even at fixed total charge and unchanged internal structure.[20] However, polymer branching does not directly capture the types of structural heterogeneity typically found in proteins or polypeptides. More generally, changes in polymer architecture are often accompanied by changes in charge density, flexibility, charge accessibility, and electrostatic interactions, making it difficult to isolate the contribution of any single parameter. Nevertheless, architectural modifications are expected to influence coacervation by altering charge presentation, conformational entropy, and the balance between intra- and intermolecular associations.

Here, we adopt an intermediate yet controlled model system based on RNA and poly-L-lysine (PLL) to investigate the influence of polycation architecture in complex coacervation. PLL–RNA complexes provide a unique balance between chemical simplicity, strong electrostatic driving forces, and biological relevance, while remaining experimentally tractable. By varying the molecular architecture of PLL through acetylation and nanoparticle formation, this approach enables us to investigate the influence of polycation architecture on complex coacervation alongside changes in effective charge density and local polymer interactions, while bridging simplified PEC models with biologically relevant condensates.

A central question we address is whether a nanoparticle-like polycation architecture and the associated changes in charge presentation hinders local charge stoichiometry at the RNA–polymer interface, thereby modulating phase behaviour and condensate properties. To test this hypothesis, we combine conventional characterization techniques for complex coacervates, including dynamic light scattering (DLS) and confocal fluorescence microscopy, with small-angle X-ray scattering (SAXS) to directly probe the internal structure of the condensates. Fluorescence lifetime measurements are further employed to provide complementary insight into the local environment and interaction dynamics within the coacervate phase.

Experimental

Materials

Poly-L-lysine hydrobromide (PLL; $M_w = 70\,000–150\,000$ g mol^{-1}), suberic acid bis(3-sulfo-*N*-hydroxysuccinimide ester) sodium salt (BS3), sodium chloride (NaCl), sodium hydroxide (NaOH), borate buffered saline (BBS, tablets), TRIS buffered saline (Tris Buffered Saline, tablets) were obtained from Sigma-Aldrich. Ribonucleic acid (RNA) from yeast was also purchased from Sigma-Aldrich (product 55714, Lot number 3994682). 2,5-Dioxopyrrolidin-1-yl acetate was obtained from BLDpharm. NHS-fluorescein (5/6-carboxyfluorescein succinimidyl ester, mixed isomers) and NHS-rhodamine (5/6-carboxytetramethylrhodamine succinimidyl ester, mixed isomers) were obtained from Thermo Fisher Scientific. The chemical structure of the molecules used is depicted in Table S1. Deionized water was obtained from a Simplicity® UV Water Purification System (Merck Millipore, Darmstadt, Germany). All reagents were used as received.

Synthesis of modified poly-L-lysine. For all modification reactions, poly-L-lysine hydrobromide was dissolved at a concentration of 3 mg mL^{-1} in borate-buffered saline (10 mM borate buffer, 0.5 M NaCl, pH 8.2) and filtered through 0.22 μm hydrophilic PTFE syringe filters (13 mm diameter) to remove pre-existing aggregates. The pH of the solution was then adjusted to 9.0 using 0.1 M NaOH.

Synthesis of partially acetylated PLL. 2,5-Dioxopyrrolidin-1-yl acetate was then added at a 70% molar ratio relative to the lysine monomer units in PLL. The reaction mixture was incubated overnight at room temperature under gentle agitation to allow for complete acetylation. Then, the solution was filtered again through 0.22 μm hydrophilic PTFE syringe. Buffer exchange was subsequently performed to replace BBS with TRIS buffer (10 mM Tris, 0.5 M NaCl, 0.1 mM EDTA, pH 7.6) using 30 kDa molecular weight cut-off centrifugal filters (Amicon Ultra), following three centrifugation cycles at 10 000 rpm for 5 minutes each. The degree of amine modification achieved under these conditions was determined to be 31%, as quantified by ^{1}H-NMR spectroscopy (Fig. S1).

Synthesis of poly-L-lysine nanoparticles (PLL-NPs). BS3 (bis(sulfosuccinimidyl) suberate) was added at a 60% molar ratio relative to the lysine monomer units in PLL. The solution was vortexed for 5 minutes at room temperature to minimize local aggregation, followed by agitation for 2 hours at room temperature. The degree of amine modification achieved under these conditions was determined to be 39%, as quantified by ^{1}H-NMR spectroscopy (Fig. S1). Then, the solution was filtered again through 0.22 μm hydrophilic PTFE syringe filters to eliminate any newly formed aggregates. Buffer exchange was then performed to replace BBS with TRIS buffer as described above.

Synthesis of fluorescently labelled PLL, PLL-NPs and RNA. Fluorescent labelling of the poly-L-lysine and RNA was performed by mixing the biopolymer solutions in TRIS buffer (10 mM TRIS, 0.5 M NaCl, 0.1 mM EDTA, pH 7.6) with NHS-rhodamine (5/6-carboxytetramethylrhodamine succinimidyl ester, mixed isomers) or NHS-fluorescein (5/6-carboxyfluorescein succinimidyl ester, mixed isomers) respectively in DMSO. The reaction was performed using sub-stoichiometric amounts of NHS-functionalized dyes relative to the estimated number of polymer chains, with the aim of obtaining on average approximately one or fewer fluorophores per chain. For PLL functionalization, 0.0528 mg NHS-rhodamine were added to 3 mg of PLL. For RNA labeling, 0.0473 mg NHS-fluorescein was added to 3 mg RNA. Since both biopolymers are polydisperse and NHS ester coupling is not expected to proceed quantitatively, the effective labeling density is expected to remain below one dye molecule per polymer chain. Labelling reactions were carried out for 1 hour at room temperature in the dark under gentle agitation. Unreacted dye was removed using Amicon Ultra centrifugal filters with a 30 kDa molecular weight cutoff. Prior to confocal imaging, fluorescence emission of the labelled samples was measured using a fluorimeter (Cary Eclipse Fluorescence Spectrometer) in order to determine optimal excitation and emission parameters for microscopy. The emission maxima used for imaging were ∼520 nm for fluorescein (excitation at 495 nm) and ∼580–590 nm for rhodamine (excitation at 552 nm), and were adjusted accordingly on the microscope settings (Fig. S4).

Coacervate formation. Coacervates were prepared by mixing aqueous stock solutions of poly-L-lysine hydrobromide and RNA, each at a nominal concentration of 3 mg mL^{-1} in Tris buffer (10 mM Tris, 0.5 M NaCl, 0.1 mM EDTA, pH 7.6). Defined volume ratios of the two stock solutions (3 : 1, 1 : 1, and 1 : 3; PLL·HBr : RNA) were combined, briefly vortexed, and allowed to equilibrate for a fixed time prior to characterization. DLS, zeta potential and confocal microscopy measurements were performed on freshly prepared samples within a couple of hours. In the case of SAXS measurements were performed on samples that had been mixed and allowed to equilibrate for longer times, typically on the order of one week.

Dynamic light scattering and zeta potential. The hydrodynamic size distributions and zeta potential of the coacervate systems were measured using a Malvern Zetasizer Nano at 25 °C, employing a 173° backscatter detection angle. For DLS measurements micro disposable cuvettes (Brand®, Sigma-Aldrich) were used and for zeta potential measurements, DTS1060 folded capillary cells (Malvern Panalytical, Sigma-Aldrich) were used. Each sample was measured in triplicate (n = 3), and the average values of hydrodynamic size distributions and zeta potential are reported.

Small-angle X-ray scattering (SAXS). The SAXS profiles were measured at 20 °C using the BioSAXS beamline BM29[21] at the European Synchrotron Radiation Facility (ESRF) in Grenoble, France. The automated sample changer loaded 50 μL for every sample into a quartz glass capillary of a diameter of 1 mm. Ten scattering frames of 1.0 s each were detected on the Pilatus 3 × 2 M detector, using an energy of 12.5 keV and a sample–detector distance of 2.827 m, measuring a q-range of 0.06–4.95 nm^{-1}, where $q = 4\pi\sin(\theta/2)/\lambda$ (θ is the scattering angle and λ the wavelength). The background sample (buffer) was measured between each sample measurement, and the capillary was cleaned between every measurement. Water was used as a primary standard to scale the data to absolute intensities. Every frame was radially averaged, checked for radiation damage followed by binning and buffer subtraction. The data is accessible in the ESRF data portal.[22]

Theoretical modeling of SAXS data

To analyze the SAXS profiles of the individual macromolecular components, two different modeling approaches were employed. The scattering from PLL and its modified derivatives was described using the generalized Debye model introduced by Hammouda, which is commonly used to represent polymer chains with fractal-like conformations:[23]

$$I(q) = I(0)\left[\frac{1}{\nu \cdot U^{\frac{1}{2\nu}}}\Gamma_{\text{inc}}\left(\frac{1}{2\nu}, U\right) - \frac{1}{\nu \cdot U^{\frac{1}{\nu}}}\Gamma_{\text{inc}}\left(\frac{1}{\nu}, U\right)\right] \quad (1)$$

where $U = \dfrac{(qR_g)^2(2\nu+2)(2\nu+1)}{6}$, ν is the scaling exponent and $\Gamma_{\text{inc}}(x, U) = \int_0^U \exp(-t)t^{x-1}\mathrm{d}t$ is the incomplete gamma function and R_g is the radius of gyration. The forward scattering, $I(0) = \phi\Delta\rho^2 V_p$, depends on the volume fraction ϕ, the volume of the scattering objects V_p, and the X-ray contrast factor $\Delta\rho^2$.

The RNA solution was analyzed with a Guinier expression as:

$$I(q) = I(0)\exp[-R_g{}^2 q^2/3] \quad (2)$$

For the coacervate samples, the scattering arising from internal chain segment correlations was described according to ref. 11 and 24 using the following Ornstein–Zernike (OZ) expression:

$$I(q)_{\text{OZ}} = \frac{I(0)}{1 + (q\xi)^2} \quad (3)$$

where the correlation length (ξ) is the blob size and $I(0)$ is the forward scattering.

The data were fitted using the SASfit program,[25] which has the above equations built-in. The fit parameter errors are given by the standard deviation errors from the least squares minimization.

Confocal fluorescence imaging and lifetime measurements. Fluorescence lifetime measurements were performed using a MicroTime 200 time-resolved confocal microscope (PicoQuant) mounted on an inverted Olympus IX71 microscope equipped with a 1.2 NA water immersion objective. Excitation was provided by a pulsed laser (485 nm) operating at a 5 MHz repetition rate with a pulse duration of approximately 180 ps (see the instrument response function [IRF] at the Fig. S5 in the SI file). To prevent photobleaching and maintain sample integrity, an average excitation power of ∼65 nW was used. For the experiments, a 5 μL droplet of the coacervate solution was deposited onto a 0.15 mm thick coverslip. The resulting fluorescence emission was separated by a non-polarized beam splitter and detected by two independent avalanche photodetectors. To facilitate dual-channel detection of the labeled components, the detectors were equipped with specific spectral filters: short-pass (550 nm) optimized for fluorescein emission and the long-pass (575 nm) for rhodamine emission. The typical photon count collected for each PL decay kinetics were higher than 500 000. Measured fluorescence decay kinetics $F(t)$ were fitted with biexponential function:

$$F(t) = A_1 \mathrm{e}^{-t/\tau_1} + A_2 \mathrm{e}^{-t/\tau_2} \quad (4)$$

where A_i and τ_i are the magnitudes and lifetimes of each exponent. For each fitted decay kinetics the reduced χ^2 was less than 2.2 × 10^{-6}, and R^2 was bigger than 0.999.

Fluorescence resonance energy transfer analysis

To estimate the fluorescence resonance energy transfer (FRET) efficiency between fluorescein and rhodamine molecules E_{FRET}, we used the equation from the ref. 26:

$$E_{\mathrm{FRET}} = 1 - {}^{\tau_{\mathrm{DA}}}\!/_{\tau_{\mathrm{D}}} \tag{5}$$

where τ_{DA} is the lifetime of fluorescein in the coacervates in the presence of rhodamine, and τ_{D} is the lifetime of fluorescein in the coacervates without the presence of rhodamine.

Results and discussion

To investigate the role of charge density and polymer architecture in coacervate formation, we first designed and characterized a set of PLL and chemically modified PLL systems. At the working pH of 7.6, well below the pK_a of PLL ($\approx$9.8),[27] all lysine residues are expected to be protonated, and the polymer behaves as a charged polycation. The synthesis and structural characterization of PLL nanoparticles have been reported previously.[28] Briefly, crosslinking was performed at pH 9 in the presence of NaCl, conditions that promote intramolecular compaction and nanoparticle formation. Following synthesis, the nanoparticles were transferred to pH 7.6, where the remaining lysine groups are protonated and the particles behave as positively charged polycations. We have to take into account that crosslinking also reduces the number of free amines and therefore lowers the effective charge density of PLL. To decouple the effect of charge density from that of architecture, we also prepared a partially acetylated PLL in which amine blocking occurs without inducing crosslinking. The degree of amine modification was chosen to yield a ζ-potential comparable to that of the PLL nanoparticles This provides a reference system with a comparable effective charge density while avoiding crosslinking-induced compaction.

Prior to coacervate formation, the individual PLL species and RNA were characterized by SAXS under dilute conditions in TRIS buffer (pH 7.6, 0.5 M NaCl), where electrostatic interactions are strongly screened and interparticle correlations are expected to be small. Fig. 1 shows the corresponding scattering profiles. The scattering curves of PLL and its modified forms were analyzed using a generalized Gaussian coil model, which appropriately describes flexible polymers in solution. In contrast, the RNA profile exhibits feature of a finite cross-section that cannot be captured by this model; therefore, a Guinier analysis was applied to estimate its radius of gyration (R_g).

The fits for linear PLL, modified PLL, and PLL-based nanoparticles reveal a progressive decrease in size upon chemical modification and nanoparticle formation. The extracted radii of gyration are R_g = 9.1 ± 0.3 nm for linear PLL, 3.9 ± 0.1 nm for modified PLL, and 2.58 ± 0.07 nm for PLL-NPs, indicating a substantial compaction of the polymer chains during nanoparticle assembly. The corresponding scaling exponents are ν = 0.73 ± 0.01 for linear PLL, 0.59 ± 0.02 for modified PLL, and 0.36 ± 0.01 for PLL-NPs. The relatively high scaling exponent observed for linear PLL is consistent with the expanded conformations typically reported for polyelectrolytes under low-salt conditions,[29] whereas the modified PLL behaves like a polymer in good solvent conditions and the PLL-NP has a more compact conformation. This size reduction confirms a structural transition from extended linear PLL chains to more compact architectures in the nanoparticle state, in agreement with our previous work.[28] Interestingly, the partially acetylated PLL exhibits also a significant reduction in R_g and ν despite the absence of cross-linking. This observation suggests that chemical modification of PLL, through reduced charge density and increased hydrophobicity, promotes chain compaction and induces significant conformational changes.

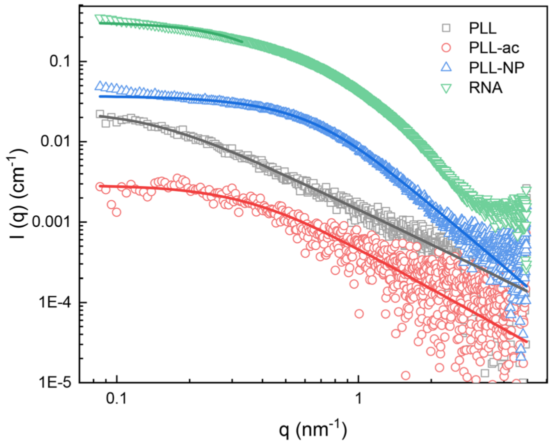

Fig. 1 SAXS profiles of macromolecules in dilute conditions 3 mg mL^{-1} in TRIS buffer pH 7.6 and 0.5 M NaCl. The solid lines correspond to fits using eqn (1) for PLL and modified PLL and eqn (2) for RNA.

On the other hand, the RNA Guinier fit yields an R_g of 4.0 ± 0.1 nm, smaller compared to the unmodified PLL linear chains but closer in size to the modified and nanoparticle PLL. The deviation from ideal Guinier behavior at the lowest q values may arise from sample polydispersity and/or weak intermolecular interactions under the high-salt conditions employed, where electrostatic repulsion between RNA molecules is expected to be strongly screened.

To investigate how different PLL architectures affect complex coacervation with RNA, coacervate samples were prepared by mixing each polycation (linear PLL, modified PLL, and PLL-based nanoparticles) with RNA at a fixed total concentration of 3 mg mL^{-1} and at varying mass ratios. Under these conditions, all systems underwent liquid–liquid phase separation, yielding dispersed RNA–PLL droplets. The resulting complexes were analyzed by dynamic light scattering and ζ-potential measurements to quantify changes in hydrodynamic size and effective electrostatic charge across different mixing ratios, as summarized in Fig. 2.

For all systems, the ζ-potential of the mixtures evolves from positive values under polycation excess to negative values under RNA excess, crossing a near-neutral region at intermediate mixing ratios. The position of this electroneutral point depends primarily on the effective charge of the polycation. Compared to linear PLL, PLL-based nanoparticles display a reduced effective

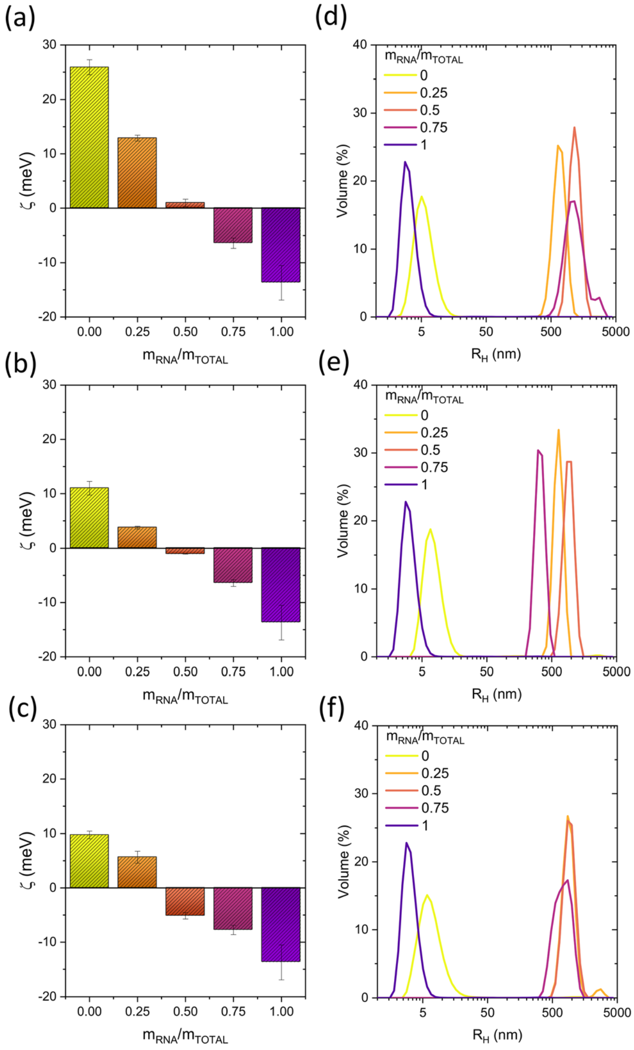

Fig. 2 Zeta potential (a–c) and hydrodynamic radius distributions (d–f) of coacervate systems formed with linear PLL (a and d), modified PLL (b and e), and PLL-NPs (c and f) at different mass ratios and a total mass concentration of 3 mg mL^{-1}.

charge, as a fraction of the primary amines is blocked during the cross-linking process. The partially acetylated PLL was introduced as a reference system in which the number of available amine groups is reduced without inducing cross-linking, leading to a lower effective charge as reflected by its ζ-potential. The PLL nanoparticles exhibit a ζ-potential comparable to that of the modified PLL under identical buffer conditions, and reach electroneutrality at similar, albeit slightly shifted, mixing ratios.

The hydrodynamic size distributions show a clear increase in droplet size near the charge-neutral region, where electrostatic stabilization is minimized. In contrast, under conditions of RNA or polycation excess, the droplet size decreases, consistent with stabilization by uncompensated charges. Coacervates formed with linear PLL are consistently larger than those formed with modified PLL or PLL-NPs, indicating that polycation modification leads to smaller droplets.

Fig. 3 shows representative confocal fluorescence microscopy images acquired in two channels, corresponding to rhodamine-labelled polycation (channel 1) and fluorescein-labelled RNA (channel 2). In all cases, strong co-localization of both components is observed within the droplets, confirming that the coacervate phase contains both RNA and PLL (or its modified forms). Only in Fig. 3h, a weak fluorescein signal is also observed in the surrounding dilute phase, which may correspond to a small fraction of uncomplexed RNA remaining outside the droplets, consistent with the slightly negative ζ-potential measured under these conditions.

The droplet size trends observed in the confocal images mirror those obtained from DLS measurements: unmodified linear PLL forms larger droplets, whereas modified PLL and PLL-NPs generate smaller and more uniform droplets. In all samples, rhodamine fluorescence is clearly observed in the regions corresponding to coacervate droplets (Fig. 3). In the linear PLL/RNA and modified PLL/RNA systems, a weak fluorescein signal is also detected in the same regions where the rhodamine intensity is maximal, consistent with coacervates formed by rhodamine-labelled PLL and fluorescein-labelled RNA. In contrast, for PLL-NPs/RNA, regions of highest rhodamine intensity coincide with a marked reduction in fluorescein emission, producing distinct dark spots in the fluorescein channel. This anti-correlation is consistent with efficient quenching of fluorescein *via* Förster resonance energy transfer (FRET) to rhodamine, a well-established donor–acceptor dye pair.[30] Thus, observed quenching indicates a reduced average separation between RNA and PLL in the PLL-NP system, reflecting a more compact local organization.

Fluorescence lifetime analysis provides a sensitive probe of nanoscale donor–acceptor proximity within the dense coacervate phase. Because the fluorescein (donor) emission spectrum overlaps efficiently with the rhodamine (acceptor) absorption spectrum, FRET is expected when the two dyes are separated by distances comparable to the Förster radius, which we estimate to be ∼6.7 nm (see SI). Under efficient FRET, an additional nonradiative relaxation pathway is introduced for the fluorescein, leading to a reduction of its measured fluorescence lifetime as the donor–acceptor separation decreases. Since fluorescein is attached to RNA and rhodamine is attached to PLL, changes in the fluorescein lifetime qualitatively report on changes in the average spatial separation between labeled RNA and PLL inside the coacervate droplets.

To quantify this effect, we measured time-resolved fluorescence decays in the fluorescein channel within concentric regions of interest defined on the confocal fluorescence images (Fig. 3), centered on individual coacervate droplets. Each fluorescence decay kinetics was fitted with a biexponential function (eqn (4)). We attribute the biexponential behaviour to two contributions: a dominant, short-lived component from fluorescein-labelled RNA in close proximity to rhodamine-labelled PLL (and therefore undergoing efficient quenching/FRET), accounting for 78–93% of the total amplitude, and a minor, longer-lived component (7–22% of the total amplitude) associated with RNA populations not tightly associated with PLL (or located further

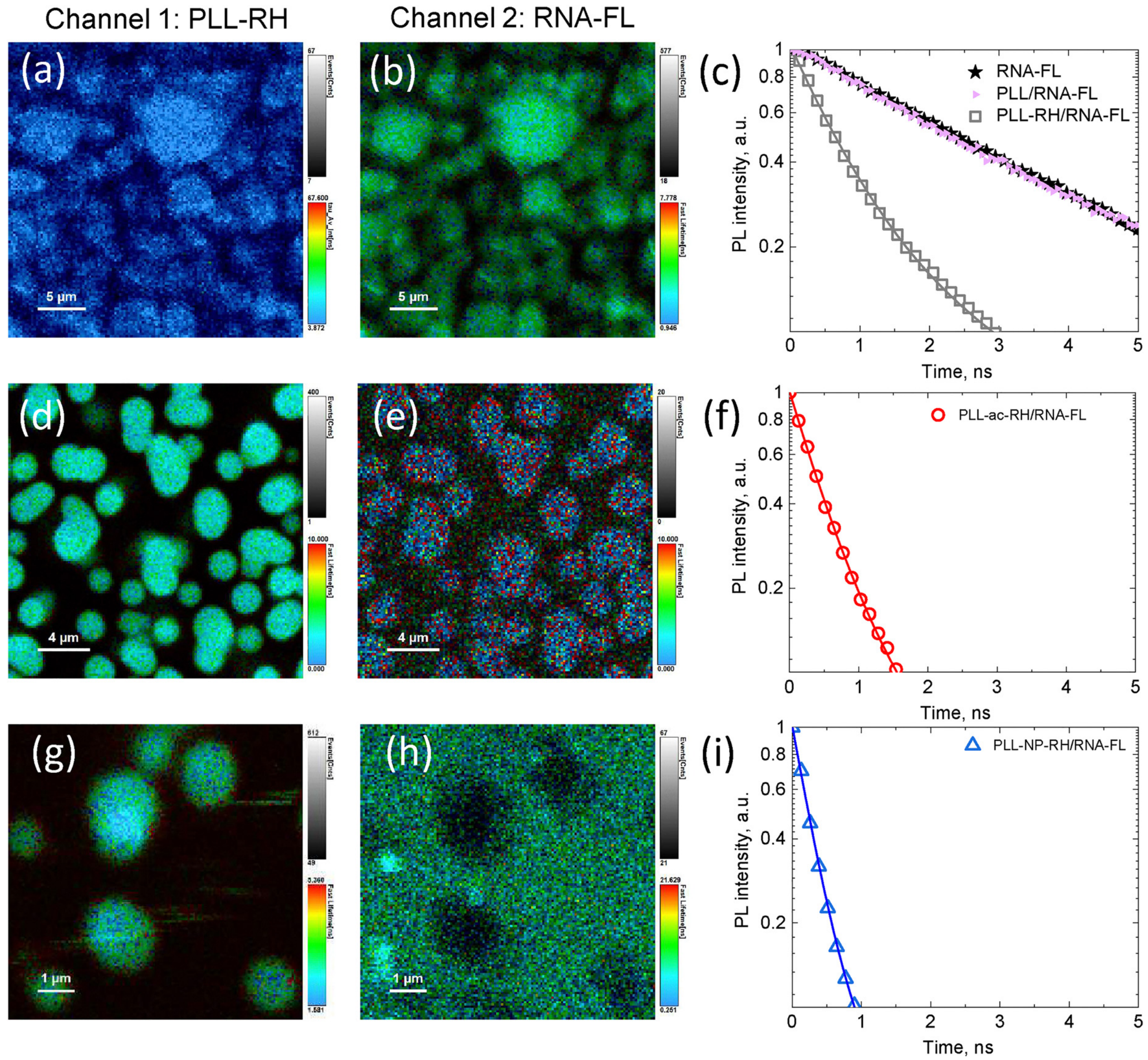

Fig. 3 Fluorescence confocal microscopy and fluorescence lifetime analysis of RNA–PLL coacervates. (a–c) Linear PLL/RNA, (d–f) modified PLL/RNA, and (g–i) PLL nanoparticle (PLL-NP)/RNA coacervates prepared at a 50 : 50 PLLHBr : RNA mass ratio. Confocal fluorescence images are shown as individual fluorescence channels: channel 1 (rhodamine-labelled PLL, panels a, d and g) and channel 2 (fluorescein-labelled RNA, panels b, e and h). The intensity scales shown to the right of each image correspond to the detected fluorescence photon counts and the color scale corresponds to the lifetime. Panels (c), (f), and (i) display the fluorescence lifetime decay curves of fluorescein-labelled RNA measured within the droplet regions for linear PLL/RNA, modified PLL/RNA, and PLL-NP/RNA coacervates, respectively, and in (c) together with a reference RNA-FL solution in the absence of PLL and in the presence of unlabelled PLL. Solid lines represent fits to eqn (4).

from rhodamine acceptors) within the probed volume. In a reference sample containing fluorescein labeled RNA without rhodamine or PLL, the fluorescence lifetime is 3.35 ns (Fig. 3c). In coacervates formed by linear PLL/RNA, the effective fluorescein lifetime decreases to 0.67 ns (Fig. 3c), evidencing efficient quenching and the formation of PLL–RNA complexes. For modified PLL/RNA, the lifetime decreases further to 0.45 ns, indicating stronger quenching and a reduced average separation between RNA and PLL. Finally, in PLL-NPs/RNA, the lifetime reaches ~0.30 ns (Fig. 3i), representing the shortest lifetime and the strongest quenching among all systems and supporting the smallest average RNA–PLL separation in the nanoparticle-based coacervates.

To evaluate whether the fluorescence lifetime reduction could instead arise from fluorescein-RNA self-quenching or homo-FRET between fluorescein molecules at high local RNA concentration, a control experiment was performed using fluorescein-labelled RNA mixed with unlabelled PLL under identical coacervate conditions. The donor-only coacervates have a similar morphology to the dually labelled ones (see Fig. S6) and exhibited fluorescence lifetimes (~3.3 ns, Fig. 3c) comparable to those of fluorescein-labelled RNA in the absence of PLL, indicating that phase separation and increased local RNA concentration alone do not produce significant lifetime shortening under the conditions studied. This supports the interpretation that the strong lifetime reductions observed in the dual-labelled systems primarily originate from interactions between fluorescein-labelled RNA and rhodamine-labelled PLL.

A fully quantitative donor–acceptor distance cannot be extracted from these lifetimes because the number and spatial distribution of rhodamine acceptors interacting with each fluorescein donor inside the coacervate phase are not known (and are unlikely to correspond to a single, well-defined donor–acceptor pair). Nevertheless, the systematic lifetime reduction from linear PLL/RNA to modified PLL/RNA and further to PLL-NPs/RNA provides robust, internal evidence for progressively tighter RNA–PLL association and a more compact local organization within the dense phase.

To corroborate this interpretation and directly access the nanoscale structure and segmental correlations within the coacervate phase, we performed small-angle X-ray scattering (SAXS) measurements on RNA complexes formed with linear PLL, modified PLL, and PLL nanoparticles. SAXS is particularly well suited to probe the internal organization of polyelectrolyte complexes, as scattering at intermediate and high scattering vectors reflects concentration fluctuations and polymer–polymer correlations within the dense phase.[11,20,31]

Fig. 4 illustrates the SAXS profiles of all coacervate systems, which exhibit a characteristic decay consistent with disordered polymer solutions arranged in larger structures. Specifically, at low q, the scattering is dominated by large-scale density fluctuations associated with the droplet structure, whereas at higher q the profiles reflect local chain correlations within the dense phase. The complete droplet scattering is not accessible within the experimental q-window due to their large sizes as observed in DLS con confocal microscopy. Thus, it is not considered in the analysis of the internal structure. To describe the internal nanoscale organization of the coacervates, the data in the intermediate- and high-q regimes were analysed using an Ornstein–Zernike (OZ) expression (eqn 3), which captures concentration fluctuations in semidilute polymer systems. From the OZ analysis, the ξ was determined to be 2.3 ± 0.1 nm for the linear PLL/RNA coacervates, 2.00 ± 0.02 nm for the modified PLL/RNA system, and 1.29 ± 0.08 nm for the PLL-NPs/RNA complex.

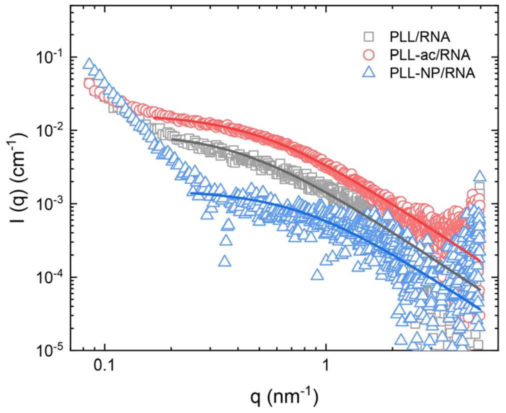

Fig. 4 Small-angle X-ray scattering (SAXS) profiles of coacervate systems: linear PLL/RNA, modified PLL/RNA, and PLL-NPs/RNA. Data were fitted using the OZ function (eqn (3)) to describe polymer conformation and internal chain correlations, from which the ξ was obtained.

The correlation lengths extracted from SAXS for the RNA–PLL coacervates lie in the nanometric range ($\xi \approx$ 1–2 nm), indicating that concentration fluctuations and segmental correlations extend over only a few nanometers within the dense phase. These values are significantly larger than those reported by Tirrell *et al.* for PLL–poly(glutamic acid) coacervates, where correlation lengths on the order of ≈0.5 nm were obtained.[11] Within the framework of semidilute polyelectrolyte scaling, such differences are attributed to variations in effective charge density, electrostatic screening and concentration in the dense phase.[32] In particular, RNA is characterized by strong counterion condensation and a highly heterogeneous charge environment, which are expected to reduce the effective charge fraction and thereby increase the correlation length at comparable polymer concentrations.[33] In addition, the presence of structured and partially double-stranded RNA regions in the yeast RNA mixture may increase the effective local thickness and heterogeneity of the polyanion compared to simpler flexible polyelectrolytes. Besides, while the dense-phase composition of complex coacervates is often relatively insensitive to the initial mixing concentration,[34,35] the lower polymer concentrations employed here, together with the intrinsic charge asymmetry of the RNA–PLL system, may alter the balance between charge compensation and counterion retention in the dense phase, further contributing to the larger correlation lengths observed.

Importantly, irrespective of the absolute magnitude of the correlation length, SAXS reveals a systematic decrease of ξ upon PLL modification, indicating a progressive tightening of the internal organization of the coacervate. Because SAXS probes total electron density fluctuations, the extracted ξ reflects the combined contribution of RNA–RNA, PLL–PLL, and RNA–PLL correlations within the dense phase rather than a single specific pair interaction. This nanoscale structural change is fully consistent with the fluorescence results, which show enhanced quenching and faster fluorescence lifetime decay upon modification, pointing to a reduced average RNA–PLL separation.

To rationalize this trend, it is important to consider that PLL modification alters more than one physicochemical aspect of the polycation that can influence the nanoscale organization of the dense phase. In both cases considered here, partial acetylation and nanoparticle formation, the effective electrostatic environment of the polycation is modified relative to linear PLL. Both modifications lead to a more compact polycation conformation relative to unmodified PLL; however, within a semidilute polyelectrolyte framework, changes in effective charge density alone would not account for the progressive decrease in the correlation length observed experimentally. In addition, nanoparticle formation introduces an additional architectural change, whereby charges are presented in a more localized and multivalent manner compared to a flexible linear chain. In fact, SAXS reveals a progressive tightening of the internal structure across the series, from linear PLL to acetylated PLL and further to PLL nanoparticles. Therefore, the observed trend cannot be attributed to electrostatics alone, suggesting that additional contributions, such as changes in solvation, desolvation entropy, and chemistry-specific enthalpic interactions introduced by polycation modification, may also play a role. These effects may further stabilize closer RNA–PLL association, consistent with the tighter nanoscale organization inferred from SAXS and the enhanced quenching and faster fluorescence lifetime decay observed experimentally. While the Ornstein–Zernike analysis captures the dominant nanoscale correlations observed under the present experimental conditions, future systematic studies as a function of salt concentration and composition may help clarify whether more complex internal structural organization emerges in these coacervates.

Conclusions

In this work, we have investigated how polycation modification and architecture influence the formation and internal organization of RNA–poly(L-lysine) coacervates. By comparing linear PLL, hydrophobically modified PLL, and compact PLL nanoparticles at comparable conditions, we were able to investigate the effects of charge density reduction and architectural compaction on both droplet-scale properties and nanoscale organization within the dense phase.

Dynamic light scattering and confocal fluorescence microscopy show that all systems form coacervates, while revealing systematic differences in droplet size and uniformity upon PLL modification. Beyond these mesoscale observations, fluorescence lifetime measurements provide direct information on local RNA–PLL proximity, showing a progressive reduction of the fluorescein lifetime from linear PLL to modified PLL and further to PLL nanoparticles. This trend reflects increasingly efficient quenching and is consistent with closer average RNA–PLL contact within the dense phase. Importantly, small-angle X-ray scattering measurements independently reveal a corresponding decrease in the correlation length, ξ, extracted from Ornstein–Zernike analysis, from linear PLL/RNA to modified PLL/RNA and PLL-NP/RNA coacervates. The reduction of ξ indicates tighter segmental correlations and enhanced local packing within the coacervate phase, providing a structural basis for the stronger quenching observed in the lifetime experiments. Together, these results establish a direct link between nanoscale concentration fluctuations probed by SAXS and the optical signatures of RNA–PLL proximity measured by fluorescence lifetime analysis.

Taken together, the combined use of confocal microscopy, fluorescence lifetime analysis, and SAXS provides complementary and converging insight into how polycation modification reshapes the internal nanoscale organization of RNA–PLL coacervates. Our results highlight that relatively subtle changes in polycation architecture can significantly alter local RNA–polymer proximity and segmental correlations within the dense phase, without changing the overall microstructural nature of the condensates. This work therefore emphasizes the importance of polymer topology as a key physical parameter in controlling the internal organization of complex coacervates and contributes to a more quantitative understanding of structure–property relationships in biomolecular condensates.

Author contributions

A. L.-F. performed the experimental work and data analysis. V. K. carried out the confocal imaging and related data analysis. A. L.-F., V. K., Y. R. and P. M. M. contributed to writing the original draft and to reviewing and editing the manuscript. P. M. M. conceived the project, supervised the work, and acquired the funding. All authors reviewed and approved the final version of the manuscript.

Conflicts of interest

There are no conflicts to declare.

Data availability

The data that support the findings of this study are available from the corresponding author upon reasonable request. Small-angle X-ray scattering (SAXS) data were collected at the European Synchrotron Radiation Facility (ESRF) and are available *via* the ESRF data portal under the corresponding experiment ID [DOI: 10.15151/ESRF-ES-2011811620].

Supplementary information (SI) is available. See DOI: https://doi.org/10.1039/d6ma00183a.

Acknowledgements

The authors are grateful to the European Synchrotron Radiation Facility, ESRF, for allocating beamtime at BM29. We would like to thank Dr Petra Pernot for assistance and support in using beamline. We also thank the University of the Basque Country (UPV/EHU) for the technical and human support provided by the SGIker NMR Service. The authors acknowledge the financial support received from Gipuzkoako Foru Aldundia, Programa Red Gipuzkoana de Ciencia, Tecnología e Innovación (2024-CIE4-000014-01), and MCIU/AEI/10.13039/501100011033 and by ERDF, EU (PID2024-159071NA-I00). This publication is part of grant RYC2024-049369-I, funded by MICIU/AEI/10.13039/501100011033 and by the FSE+. We used an AI-assisted language model to improve grammar and clarity. All interpretations and conclusions are those of the authors.

References

1 T. Hirose, K. Ninomiya, S. Nakagawa and T. Yamazaki, *Nat. Rev. Mol. Cell Biol.*, 2023, **24**, 288–304.
2 A. Drino and M. R. Schaefer, *BioEssays*, 2018, **40**, 1800085.
3 A. L. Darling, Y. Liu, C. J. Oldfield and V. N. Uversky, *Proteomics*, 2018, **18**, 1700193.
4 E. P. Bentley, B. B. Frey and A. A. Deniz, *Chem. – Eur. J.*, 2019, **25**, 5600–5610.

5 S. Alberti, A. Gladfelter and T. Mittag, *Cell*, 2019, **176**, 419–434.

6 C. E. Sing and S. L. Perry, *Soft Matter*, 2020, **16**, 2885–2914.

7 N. Martin, *ChemBioChem*, 2019, **20**, 2553–2568.

8 A. Sathyavageeswaran, J. Bonesso Sabadini and S. L. Perry, *Acc. Chem. Res.*, 2024, **57**, 386–398.

9 D. Oupický, A. L. Parker and L. W. Seymour, *J. Am. Chem. Soc.*, 2002, **124**, 8–9.

10 J. L. Paris, R. Gaspar, F. Coelho, P. A. A. De Beule and B. F. B. Silva, *ACS Nano*, 2023, **17**, 17587–17594.

11 A. B. Marciel, S. Srivastava and M. V. Tirrell, *Soft Matter*, 2018, **14**, 2454–2464.

12 L. Li, S. Srivastava, M. Andreev, A. B. Marciel, J. J. de Pablo and M. V. Tirrell, *Macromolecules*, 2018, **51**, 2988–2995.

13 A. M. Rumyantsev, E. B. Zhulina and O. V. Borisov, *Macromolecules*, 2018, **51**, 3788–3801.

14 A. E. Neitzel, Y. N. Fang, B. Yu, A. M. Rumyantsev, J. J. de Pablo and M. V. Tirrell, *Macromolecules*, 2021, **54**, 6878–6890.

15 A. Agrawal, Y. N. Fang, S. Rizvi, N. F. Noor Azman, M. V. Tirrell, A. Karim and A. E. Neitzel, *Macromolecules*, 2025, **58**, 7776–7787.

16 T. Ukmar-Godec, S. Hutten, M. P. Grieshop, N. Rezaei-Ghaleh, M.-S. Cima-Omori, J. Biernat, E. Mandelkow, J. Söding, D. Dormann and M. Zweckstetter, *Nat. Commun.*, 2019, **10**, 2909.

17 F. P. Cakmak, S. Choi, M. O. Meyer, P. C. Bevilacqua and C. D. Keating, *Nat. Commun.*, 2020, **11**, 5949.

18 L.-W. Chang, T. K. Lytle, M. Radhakrishna, J. J. Madinya, J. Vélez, C. E. Sing and S. L. Perry, *Nat. Commun.*, 2017, **8**, 1273.

19 B. M. Johnston, C. W. Johnston, R. A. Letteri, T. K. Lytle, C. E. Sing, T. Emrick and S. L. Perry, *Org. Biomol. Chem.*, 2017, **15**, 7630–7642.

20 K. C. Stevens and M. V. Tirrell, *ACS Macro Lett.*, 2024, **13**, 688–694.

21 M. D. Tully, J. Kieffer, M. E. Brennich, R. Cohen Aberdam, J. B. Florial, S. Hutin, M. Oscarsson, A. Beteva, A. Popov, D. Moussaoui, P. Theveneau, G. Papp, J. Gigmes, F. Cipriani, A. McCarthy, C. Zubieta, C. Mueller-Dieckmann, G. Leonard and P. Pernot, *J. Synchrotron Radiat.*, 2023, **30**, 258–266.

22 P. Blesio, A. L. Cortajarena and P. Malo de Molina, *Structural Characterization of Consensus TetratricoPeptide Repeat (CTPR) Protein Nanoparticles via SAXS*, https://doi.esrf.fr/10.15151/ESRF-ES-2011811620.

23 B. Hammouda, *Polymer Characteristics*, Springer-Verlag, Berlin/Heidelberg, 2005, pp. 87–133.

24 Y. N. Fang, A. M. Rumyantsev, A. E. Neitzel, H. Liang, W. T. Heller, P. F. Nealey, M. V. Tirrell and J. J. de Pablo, *Proc. Natl. Acad. Sci. U. S. A.*, 2023, **120**(32), e2302151120.

25 I. Breßler, J. Kohlbrecher and A. F. Thünemann, *J. Appl. Crystallogr.*, 2015, **48**, 1587–1598.

26 J. R. Lakowicz, *Principles of Fluorescence Spectroscopy*, Springer US, Boston, MA, 2006, pp. 443–475.

27 A. Dos, V. Schimming, S. Tosoni and H.-H. Limbach, *J. Phys. Chem. B*, 2008, **112**, 15604–15615.

28 T. P. Le, J. Kohlbrecher and P. Malo de Molina, *ChemRxiv*, 2025, preprint, DOI: 10.26434/chemrxiv-2025-nzp8j.

29 E. Buvalaia, M. Kruteva, I. Hoffmann, A. Radulescu, S. Förster and R. Biehl, *ACS Macro Lett.*, 2023, **12**, 1218–1223.

30 P. G. Wu and L. Brand, *Anal. Biochem.*, 1994, **218**, 1–13.

31 E. Spruijt, F. A. M. Leermakers, R. Fokkink, R. Schweins, A. A. van Well, M. A. Cohen Stuart and J. van der Gucht, *Macromolecules*, 2013, **46**, 4596–4605.

32 A. V. Dobrynin and M. Rubinstein, *Prog. Polym. Sci.*, 2005, **30**, 1049–1118.

33 J. Lipfert, S. Doniach, R. Das and D. Herschlag, *Annu. Rev. Biochem.*, 2014, **83**, 813–841.

34 E. Spruijt, A. H. Westphal, J. W. Borst, M. A. Cohen Stuart and J. van der Gucht, *Macromolecules*, 2010, **43**, 6476–6484.

35 D. Priftis and M. Tirrell, *Soft Matter*, 2012, **8**, 9396–9405.